Article

How Does Scale Effect Influence Spring Vegetation Phenology Estimated from Satellite-Derived Vegetation Indexes?

Licong Liu [1], Ruyin Cao [2,*], Miaogen Shen [3], Jin Chen [1], Jianmin Wang [4] and Xiaoyang Zhang [4]

[1] State Key Laboratory of Earth Surface Processes and Resource Ecology, Faculty of Geographical Science, Beijing Normal University, Beijing 100875, China; liulicong@mail.bnu.edu.cn (L.L.); chenjin@bnu.edu.cn (J.C.)

[2] School of Resources and Environment, University of Electronic Science and Technology of China, 2006 Xiyuan Avenue, West Hi-tech Zone, Chengdu 611731, China

[3] Key Laboratory of Alpine Ecology, Institute of Tibetan Plateau Research, CAS Center for Excellence in Tibetan Plateau Earth Sciences, Chinese Academy of Sciences, 16 Lincui Road, Beijing 100101, China; shenmiaogen@itpcas.ac.cn

[4] Geospatial Sciences Center of Excellence, Department of Geography and Geospatial Sciences, South Dakota State University, Brookings, SD 57007, USA; Jianmin.Wang@sdstate.edu (J.W.); xiaoyang.zhang@sdstate.edu (X.Z.)

* Correspondence: cao.ruyin@uestc.edu.cn; caoruyin119@gmail.com

Abstract: As an important land-surface parameter, vegetation phenology has been estimated from observations by various satellite-borne sensors with substantially different spatial resolutions, ranging from tens of meters to several kilometers. The inconsistency of satellite-derived phenological metrics (e.g., green-up date, *GUD*, also known as the land-surface spring phenology) among different spatial resolutions, which is referred to as the "scale effect" on *GUD*, has been recognized in previous studies, but it still needs further efforts to explore the cause of the scale effect on *GUD* and to quantify the scale effect mechanistically. To address these issues, we performed mathematical analyses and designed up-scaling experiments. We found that the scale effect on *GUD* is not only related to the heterogeneity of *GUD* among fine pixels within a coarse pixel, but it is also greatly affected by the covariation between the *GUD* and vegetation growth speed of fine pixels. *GUD* of a coarse pixel tends to be closer to that of fine pixels with earlier green-up and higher vegetation growth speed. Therefore, *GUD* of the coarse pixel is earlier than the average of *GUD* of fine pixels, if the growth speed is a constant. However, *GUD* of the coarse pixel could be later than the average from fine pixels, depending on the proportion of fine pixels with later *GUD* and higher growth speed. Based on those mechanisms, we proposed a model that accounted for the effects of heterogeneity of *GUD* and its co-variation with growth speed, which explained about 60% of the scale effect, suggesting that the model can help convert *GUD* estimated at different spatial scales. Our study provides new mechanistic explanations of the scale effect on *GUD*.

Keywords: land surface phenology; scale effect; spatial heterogeneity; spring phenology; spatial resolution; vegetation index; vegetation growth speed

1. Introduction

Land-surface phenology, reflecting the seasonality of vegetated land surface detected by remotely sensed imagery, has attracted increasing attention in recent decades, as it provides an independent, long-term, globally sensed measure for assessing ecosystem responses to climate change [1–3]. Although significant progress has been made to detect phenology metrics, particularly

the green-up date (*GUD*), based on vegetation index (*VI*) time-series, there is still considerable inconsistency in the detected land-surface phenology among different sensors [3–5], thus posing challenges in the precise quantification of vegetation phenological changes and their responses to climate change at a large scale. The inconsistency may be caused by differences in imaging condition, spectral response functions of sensors and geometric registration. It can also be caused by the difference of spatial resolutions of employing *VI*, data because sensors with different spatial resolutions observe vegetation at various scales, ranging from individual species to complex landscapes that consist of various vegetation types and phenological timings.

Previous studies have found that the value of a phenological metric at coarse resolution is not necessarily equal to the average of the metric at fine resolution for the same footprint, which is known as the "scale effect" [5,6]. Understanding how the scale effect influences land-surface phenology detection is becoming a fundamental point for cross-scale comparisons and validation of phenology metrics against field observations [5–7].

Generally, the scale effect arises from the heterogeneity of a land surface that contains various compositions of plant species and/or land-cover types (both can be regarded as endmembers in spectral mixture models), and these species or land-cover types differ in terms of phenological metrics [1,5,8–11]. Three main questions arise with regard to cross-scale comparisons and ground-based validation of phenology metrics and their changes. (1) Is there a systematic difference in the detected phenology by using *VI* datasets with different spatial resolutions? (2) What are the factors accounting for the scale effect? (3) How do these factors contribute to the scale effect? Several studies have made valuable attempts to answer these questions.

As for the first question, previous studies have confirmed differences in detected *GUD*s between sensors with different spatial resolutions. Fisher and Mustard [12] compared the *GUD* from Moderate-resolution Imaging Spectroradiometer (MODIS) with the average of *GUD* of corresponding Landsat pixels. The difference between them ranged from 0 to more than 25 days, but no systematic difference was found. Zhang et al. [5] compared *GUD* from 30-m Landsat-MODIS fused data with that from 450-m Visible Infrared Imaging Radiometer data and found that the *GUD* at the coarser scale is only about 30 percentile of the *GUD* in corresponding fine pixels. However, Peng et al. [7] showed that the percentile value varied substantially across different landscapes and ecosystems. Obviously, changes in the percentile values are expected because of the presence of spatiotemporal variations in the distribution of *GUD* values of fine pixels within a coarse pixel. Therefore, the question of whether there is a systematic difference in detected phenology by using datasets with different spatial resolutions still needs to be clarified.

With regard to the second and third questions, surface heterogeneity of vegetation types (or endmembers) of fine pixels within a coarse pixel is an obvious source of the scale effect. Several studies found that there is a strong correlation between surface heterogeneity and the scale effect. Fisher and Mustard [12] suggested that high spatial variability of vegetation within MODIS pixels may have caused the difference between MODIS *GUD* and the average *GUD* of corresponding Landsat pixels. This result was further supported by later studies. Zhang et al. [5] showed that the scale effect is associated with the heterogeneity of *GUD* values, but did not describe a mechanism. Moreover, based on a mixed pixel simulation experiment, Chen et al. [11] demonstrated that, in addition to changes in fractions of endmembers and in *GUD* values of endmembers in a coarse pixel, the *GUD* of a coarse pixel could be greatly changed by annual maximum values of fine *VI* times-series. These findings suggest that the scale effect is not simply caused by the heterogeneity of vegetation types or *GUD* values of fine pixels within a coarse pixel. Thus, despite previous exploration of potential factors affecting the scale effect, the mechanism underlying it is still not clear.

In this study, we systematically investigated the factors that may influence the scale effect and further developed a multivariate scale-effect model to account for bias of *GUD* among different spatial resolutions. Our aims were two-fold: (1) to assess whether there are systematic differences in *GUD* among different scales caused by those factors; and (2) to identify the mathematical relationship between the scale effect and the factors.

2. Theoretical Analyses of the Scale Effect of *VI* on GUD Detection by Using Two-Endmember Scenarios

2.1. Defining GUD in VI Time-Series

We determined *GUD* by using Zhang's logistic method [13], because it has been employed in MODIS land-surface phenology products [2]. To be exact, we first used the four-parameter logistic function to fit the *VI* time-series during a rising period, which is from the start of a year to the date when the annual maximum *VI* occurs:

$$VI_{fit}(t) = \frac{C}{1 + e^{a+bt}} + d \tag{1}$$

where t is the day of year (DOY), and $VI_{fit}(t)$ is the fitted VI value at t. The parameter c represents the difference between annual maximum and minimum VI values, and d is the background VI value. The parameter a controls the translation of the time-series and parameter b is associated with the rate of VI increase.

Then, from the fitted logistic curve of Equation (1), the curvature (K) of $VI_{fit}(t)$ can be calculated as:

$$K = \frac{VI_{fit}(t)''}{(1 + (VI_{fit}(t)')^2)^{3/2}} \tag{2}$$

Thus, the *GUD* is defined as the date when the rate of change of the K reaches its first local maximum value. Note that $VI_{fit}(t)'$ and $VI_{fit}(t)''$ are the first and second order derivatives of $VI_{fit}(t)$ with respect to t, K is thus independent of the constant addition item d (the background values of *VI* times-series). As a result, *GUD* is determined by the parameters a, b, and c.

2.2. Defining the Scale Effect of VI on GUD Estimation

The *GUD* at a coarse pixel (GUD_{coarse}) was directly estimated from the *VI* time-series of the coarse pixel. To compare GUD_{coarse} with the *GUD* of fine pixels (GUD_{fine}) at a same footprint, we aggregated GUD_{fine} covered by the coarse pixel through averaged approach (calculating the unweighted average of GUD_{fine}) as suggested by Peng et al. [7]. The result was noted as $GUD_{fine-ave}$. Thus, we evaluated the scale effect of *GUD* using the difference between GUD_{coarse} and $GUD_{fine-ave}$, expressed as:

$$Bias = GUD_{coarse} - GUD_{fine-ave} \tag{3}$$

Given that *GUD* is estimated from the logistic function, we can infer that GUD_{coarse} is controlled by its own fitting parameters a_{coarse}, b_{coarse}, and c_{coarse}, and the $GUD_{fine-ave}$ is determined by the fitting parameters (i.e., a_{fine}, b_{fine}, and c_{fine}) of fine *VI* time-series. Then, we used the linear mixing model of *VI* times series to link the parameters at different scale, that is, the *VI* at a coarse pixel (VI_{coarse}) is assumed to be a linear mixture of the total number of *VIs* at fine pixels within the coarse pixel, expressed as:

$$VI_{coarse} = \frac{1}{n}\sum_{i=1}^{n} VI_{fine}^i \tag{4}$$

where n is the number of fine pixels within the coarse pixel. Although the normalized difference vegetation index (*NDVI*) value of a coarse pixel tends to be slightly lower than the average of *NDVI* of corresponding fine pixels [14], it only introduces small errors when modeling the coarse *VI* time-series (i.e., EVI time-series) from fine pixels by a linear mixture model [6,15,16]. Based on Equation (4), parameters a_{coarse}, b_{coarse}, and c_{coarse} of a coarse *VI* time-series are closely related to the corresponding fine *VI* time-series and their parameters (i.e., a_{fine}, b_{fine}, and c_{fine}). Thus, the bias value in Equation (3) is a function (*f*) of the controlling parameters of fine pixels, expressed as:

$$Bias = f(a_{fine}, b_{fine}, c_{fine}) \tag{5}$$

2.3. Factors Influencing the Scale Effect on GUD Estimation

To clarify the key factors influencing the scale effect of *GUD* estimation, we first investigated the two-pixel mixture case. As suggested in Section 2.2, the scale effect can be expressed as:

$$Bias = f(a_{\text{fine},1}, , b_{\text{fine},1}, c_{\text{fine},1}, a_{\text{fine},2}, , b_{\text{fine},2}, c_{\text{fine},2}) \tag{6}$$

Considering that the parameters *a*, *b* and *c* are less intuitive, we replaced them by using *GUD*, length of the period (*MP*) from *GUD* to maturity date (*MD*) and greenness change (*GC*). Here, the maturity date was calculated as the date when the rate of change of the curvature of a logistic function fitted by *VI* time series reaches the second local maximum value from the start of a year [13]. The *GC* is defined as the difference between minimum *VI* before *GUD* and annual maximum *VI* (See Figure 1). According to Shang et al. [17], the parameters *a*, *b*, and *c* can be expressed by *GUD*, *MP*, and *GC*, as (details are given in Appendix A):

$$a = log\_e(5 + 2\sqrt{6}) \times \left(1 + \frac{2GUD}{MP}\right)$$

$$b = \frac{-2 \times lo\,g_e(5 + 2\sqrt{6})}{MP}$$

$$c = GC \tag{7}$$

The meanings of the parameters *GUD*, *MP* and *GC* are easy to understand. The *MP* and *GC* represent the growth speed of *VI*, defined as the amount of increasing in *VI* per unit time, at the horizontal axis (time required) and vertical axis (the range of *VI*). Therefore, the *Bias* in the left of Equation (1) can be represented as a function of *GUD*, *MP* and *GC*, and Equation (6) can be rewritten as:

$$Bias = f(GUD_{\text{fine},1}, MP_{\text{fine},1}, GC_{\text{fine},1}, GUD_{\text{fine},2}, MP_{\text{fine},2}, GC_{\text{fine},2}) \tag{8}$$

Previous studies have suggested that the scale effect is mainly caused by the difference among fine pixels within a coarse pixel [5,6,18]. Based on Equation (8), we therefore assume that the bias is mainly influenced by the difference in the parameters between two fine pixels (i.e., ΔGUD_{fine}, ΔMP_{fine}, and ΔGC_{fine}). Thus, Equation (8) becomes:

$$Bias = f(\Delta GUD_{fine}, \Delta MP_{fine}, \Delta GC_{fine}) \tag{9}$$

The three factors (ΔGUD_{fine}, ΔMP_{fine} and ΔGC_{fine}) are considered as the biophysical factors that influence the *GUD* at coarse pixels, which is illustrated in Figure 1.

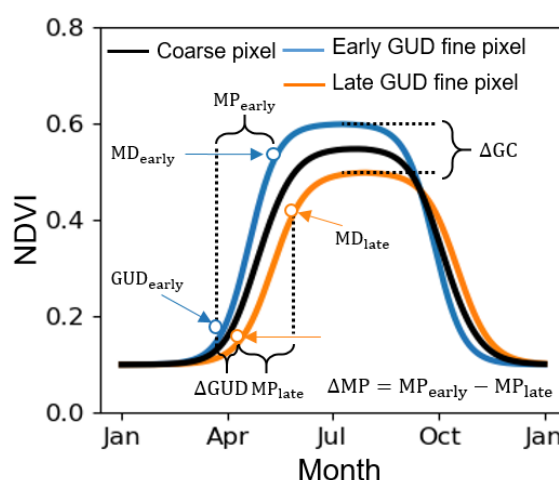**Figure 1.** Illustration of three factors (ΔGUD_{fine}, ΔMP_{fine}, ΔGC_{fine}) for a composite case in which the coarse pixel contains two fine pixels. Two fine pixels were represented as the double-logistic curves to illustrate the whole vegetation index (*VI*) time-series of vegetation. MD refers to the maturity date.

2.4. Form of Function f in Equation (9)

We divided the function *f* in Equation (9) into two parts: (1) the bias caused only by ΔGUD_{fine}, and (2) the bias caused by heterogeneity of growth speed at a given ΔGUD_{fine}, expressed as:

$$Bias = bias_{\Delta GUD_{\text{fine}}} + bias_{\Delta MP_{\text{fine}}, \Delta GC_{\text{fine}} | \Delta GUD_{\text{fine}}} \tag{10}$$

For simplicity, we assume that the effects of ΔMP_{fine} and ΔGC_{fine} on *Bias* are independent of each other, so Equation (10) can be rewritten as:

$$Bias = bias_{\Delta GUD_{\text{fine}}} + bias_{\Delta MP_{\text{fine}} | \Delta GUD_{\text{fine}}} + bias_{\Delta GC_{\text{fine}} | \Delta GUD_{\text{fine}}} \tag{11}$$

To be strict, the effects of ΔMP_{fine} and ΔGC_{fine} may not be independent and thus there may be interactions between ΔMP_{fine} and ΔGC_{fine} at a certain ΔGUD_{fine}. However, incorporating the interaction effect could make the scale-effect model more complicated and difficult to parameterize. We thus employed the three main items in Equation (11) and investigated the performance of the model in explaining the scale effect.

We explored the possible function forms of each item in Equation (11) by conducting simulation experiments for three scenarios. In scenario I, we simulated two *VI* curves for the fine pixel 1 and pixel 2 with different *GUD* but identical *MP* and *GC*. We assumed that *GUD* for pixel 1 was fixed DOY 110, whereas the *GUD* of pixel 2 varied between DOY 90 and 130 (the *GUD* difference changes from −20 to 20 days), which was used to analyze variation in ΔGUD_{fine} (Figure 2a). This scenario shows that $bias_{\Delta GUD_{\text{fine}}}$ values varies with ΔGUD_{fine} in a quadratic function (Figure 2d):

$$bias_{\Delta GUD_{\text{fine}}} = c_1 \Delta GUD_{\text{fine}}^2 \tag{12}$$

where c_1 is the fitting parameter. Negative bias in Figure 2d suggests an advanced GUD_{coarse} caused by the scale effect, indicating that ΔGUD_{fine} between fine pixels will lead to an earlier GUD_{coarse}.
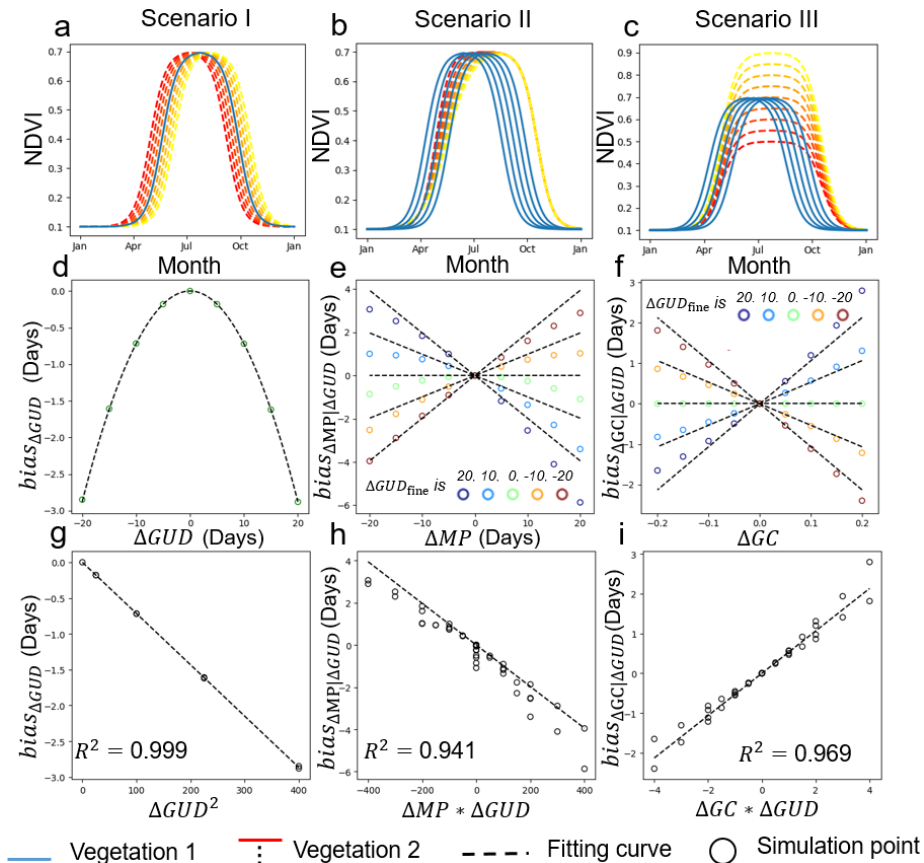
Figure 2. Results of the simulation experiments (three scenarios) exploring the function forms of three variables in Equation (11). (**a**–**c**) *VI* Curves 1 (blue) and 2 (red to yellow) in Scenarios I, II, and III. (**d**–**f**) $bias_{\Delta GUD_{fine}}$, $bias_{\Delta MP_{fine}|\Delta GUD_{fine}}$, and $bias_{\Delta GC_{fine}|\Delta GUD_{fine}}$ change with the corresponding factors. The negative values of ΔMP_{fine} and positive ΔGC_{fine} indicate faster growth speed of pixel 1 than that of pixel 2. The different color of point refers to different levels of ΔGUD_{fine} (i.e., −20, −10, 0,10 and 20 days) and the negative ΔGUD_{fine} values indicate earlier green-up date (*GUD*) of pixel 1 than that of pixel 2. The dashed lines represent the proposed function forms (Equations (12) and (13)) used to fit these bias values. (**g**–**i**) Fitting performance of each function form, respectively.

In scenario II, we investigated the effect of ΔMP_{fine} on bias ($bias_{\Delta MP_{fine}|\Delta GUD_{fine}}$) at different levels of ΔGUD_{fine} (Figure 2b). The *MP* in pixel 1 was fixed at 75 days, whereas that of pixel 2 changed from 55 to 95 days to simulate different ΔMP_{fine} values (−20 to 20 days). In addition, we set the *GUD* of pixel 1 from DOY 90 to 130 and fixed the *GUD* in pixel 2 at DOY 110 to simulate different levels of ΔGUD_{fine} (−20, −10, 0, 10, 20 days). As shown in Figure 2e, at a given level of ΔGUD_{fine}, the bias caused by ΔMP_{fine} approximately follows a linear function. In addition, a greater effect of ΔMP_{fine} on bias is observed when ΔGUD_{fine} is larger (Figure 2h). Scenario III (Figure 2c) was the same scenario II but for ΔGC_{fine}. Similarly, we obtained linear functions between the bias and ΔGC_{fine} (Figure 2f). Based on these observations, we used the following equations to describe their effect in scenarios II and II:

$$bias_{\Delta MP_{fine}|\Delta GUD_{fine}} = c_2 \Delta GUD_{fine} \times \Delta MP_{fine}$$

$$bias_{\Delta GC_{fine}|\Delta GUD_{fine}} = c_3 \Delta GUD_{fine} \times \Delta GC_{fine} \qquad (13)$$

where c_2 and c_3 are the fitting parameters.

The linear fitting using Equation (13) achieved R^2 values of 0.941 and 0.969 for these variables (Figure 2h,i); the former ($\Delta GUD_{fine} \times \Delta MP_{fine}$) showed a negative slope and the latter ($\Delta GUD_{fine} \times \Delta GC_{fine}$) had a positive slope. Note that a smaller *MP* and a greater *GC* both indicate a greater growth speed. The form of Equation (13) suggests that the synchronous change of *GUD* and growth speed (i.e., positive sign of $\Delta GUD_{fine} \times \Delta GC_{fine}$) can delay GUD_{coarse} and vice versa.

In summary, given that the *GUD* is derived from the *VI* curve in the logistic-form, results of the simulation experiments suggest that heterogeneity of ΔGUD_{fine} leads to an earlier GUD_{coarse}, and this advance in GUD_{coarse} is further adjusted by the relationship between ΔGUD_{fine} and ΔMP_{fine} or ΔGC_{fine}, which can enhance or offset the negative bias in GUD_{coarse} depending on the reversal and synchronous changes between the *GUD* and growth speed. Further, it can be deduced that the detected *GUD* of a coarse pixel is closer to the fine pixel with an earlier *GUD* and a faster growth speed (shorter *MP* and greater *GC*).

By combining Equations (11)–(13), we achieved the final model for estimating the scale effect of *GUD* for the two-endmember case:

$$Bias = c_1 \Delta GUD_{fine}^2 + c_2 \Delta GUD_{fine} \times \Delta MP_{fine} + c_3 \Delta GUD_{fine} \times \Delta GC_{fine} \qquad (14)$$

Following the function form, we generalized Equation (14) for the multi-endmember case by using variance and covariance (i.e., var_{GUD}, $cov_{MP,GUD}$, and $cov_{GC,GUD}$ instead of ΔGUD_{fine}^2, $\Delta GUD_{fine} \times \Delta MP_{fine}$, and $\Delta GUD_{fine} \times \Delta GC_{fine}$, respectively):

$$Bias = c_1 var_{GUD_{fine}} + c_2 cov_{MP_{fine},GUD_{fine}} + c_3 cov_{GC_{fine},GUD_{fine}} \qquad (15)$$

Next, we describe a series of experiments designed to test Equations (14) and (15).

3. Experimental Design

3.1. Simulation Experiments Based on PhenoCam Sites Data

3.1.1. Phenology Observations

We collected some typical vegetation greenness annual curves from eight phenological camera observation sites (Table 1) provided by the PhenoCam website [19]

(https://phenocam.sr.unh.edu/webcam/). PhenoCam data were used because digital photographs at the ground were cloud-free and were taken repeatedly at a high temporal frequency (e.g., 0.5 h). We calculated the green chromatic coordinate (*GCC*) and used it as the indicator of land-surface greenness, according to previous studies [20–22]:

$$GCC = \frac{G}{R + G + B} \tag{16}$$

where *R*, *G*, and *B* represent digital numbers at the red, green, and blue bands, respectively. We generated the time-series of *GCC* to represent the annual greenness change of vegetation at each site (Figure 3).
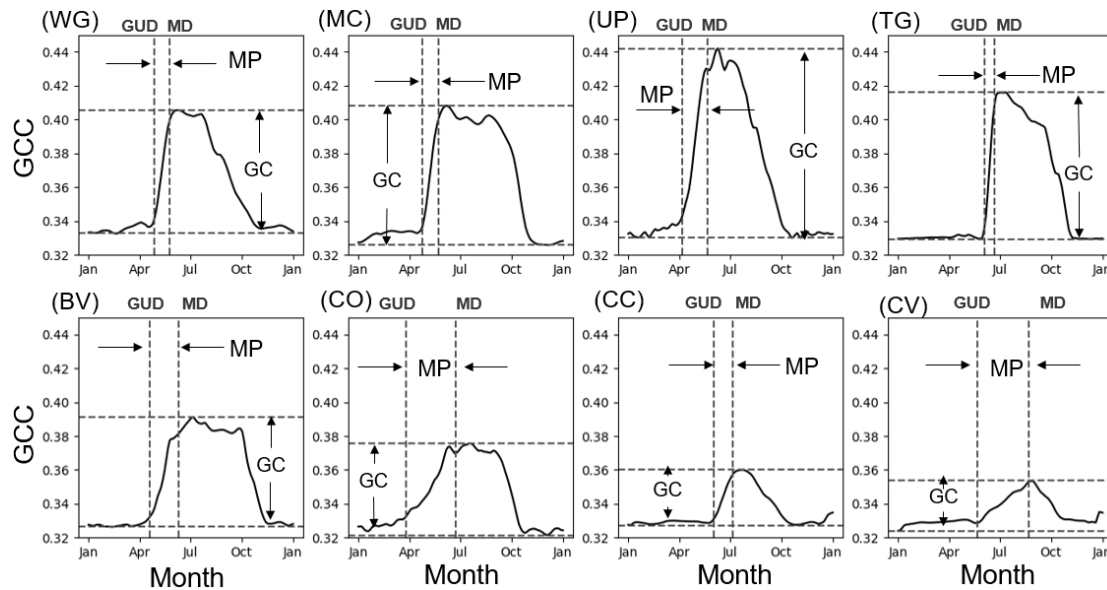
Figure 3. Green chromatic coordinate (*GCC*) curves of eight vegetation sites derived from PhenoCam data. The vegetation type at each site (identification (ID) in parentheses) is listed in Table 1.

Table 1. Details of the eight sites where data were gathered for *GCC* curves used for the simulation. The abbreviations of vegetation types are switchgrass (SG), miscanthus (MC), grassland (GR), deciduous needleleaf (DN), deciduous broadleaf (DB), mixed vegetation (MX), shrubs (SH), and tundra (TN).

Site ID	Site Name	Type	Year	Longitude	Latitude	*GUD*	*MP*	*GC*
WG	uiefswitchgrass	SG	2014	−88.197	40.064	118.2	28.0	0.073
MC	uiefmiscanthus	MC	2012	−88.198	40.063	116.2	28.2	0.082
UP	uiefprairie	GR	2011	−88.197	40.064	98.1	45	0.112
TG	torgnon-ld	DN	2013	7.561	45.824	156.0	16.9	0.087
BV	bitterootvalley	DB	2014	−114.091	46.507	110.3	51.8	0.065
CO	canadaOBS	MX	2012	−105.118	53.987	86.4	88.1	0.054
CC	contactcreek	SH	2012	−155.923	58.208	154.6	32.7	0.033
CV	coville	TN	2011	−155.563	58.803	141.7	92.3	0.030

3.1.2. Testing the Two-Endmember Model

We used the PhenoCam data to test the two-endmember model in Equation (14). For this, we repeatedly chose two curves from the eight *GCC* curves (Figure 3) at each time, which generated a total of 28 combinations. In each combination, we first mixed the two curves (GCC_{fine}) with equal proportions to simulate the *GCC* curve of a coarse pixel (GCC_{coarse}) according to Equation (4). We then calculated ΔGUD_{fine}, ΔMP_{fine}, and ΔGC_{fine} between the two GCC_{fine} curves. The bias, as an indicator of the scale effect (Equation (3)), was calculated as the difference between the *GUD* of GCC_{coarse} and the average of *GUD* of the two GCC_{fine} curves. The model includes three influential

factors (ΔGUD_{fine}, ΔMP_{fine}, and ΔGC_{fine}), so for comparison, we also performed linear fitting at each time by only employing one factor. Finally, the bias values in all 28 combinations were fitted by the proposed two-endmember model and the one factor linear model, respectively. Because different equations may have different numbers of parameters, we calculated the adjusted R^2 and root-mean-square error (RMSE) for evaluations.

3.1.3. Testing the Multi-Endmember Model Based on SIMMAP Simulated Data

We tested the multi-endmember model by using the data simulated by the SIMMAP (simulación de mapas) software [23]. The software can generate landscape spatial patterns that contain various categories of different degrees of landscape fragmentation based on the modified random cluster method. The degrees of landscape fragmentation were control by parameter *p*, which was defined as the initial probability that a pixel was marked. The larger the *p* parameter, the smaller the number of patches and the more homogeneous the surface (as shown in Figure 4). More detailed descriptions and download links of SIMMAP can be found on the website: http://www2.montes.upm.es/personales/saura/software.html.

We first generated three images (1000 × 1000 pixels) as fine resolution images with different degrees of landscape fragmentation, controlled by the parameter *p* in SIMMAP (*p* = 0.45, 0.50, 0.55; Figure 4). In each image, we included the eight vegetation types with equal proportion, and for each type a PhenoCam *GCC* curve (Table 1) was assigned. We then scaled up the three fine resolution images to coarser with aggregation rates of 3 × 3, 4 × 4, …, 20 × 20 pixels (Figure 5a,b) based on Equation (4). GUD_{coarse}, corresponding $GUD_{\text{fine}-\text{ave}}$, and three model parameters (i.e., the variance and covariance) were then calculated from coarse and fine resolution images (Figure 5c,d). The bias values were thus calculated as the difference of GUD_{coarse} and $GUD_{\text{fine}-\text{ave}}$. Finally, we tested our multi-endmember model on bias at each scale respectively. Note that we randomly split all of the pixels into two-thirds for training (determining the three coefficients in Equation (15)) and one-third for validation.
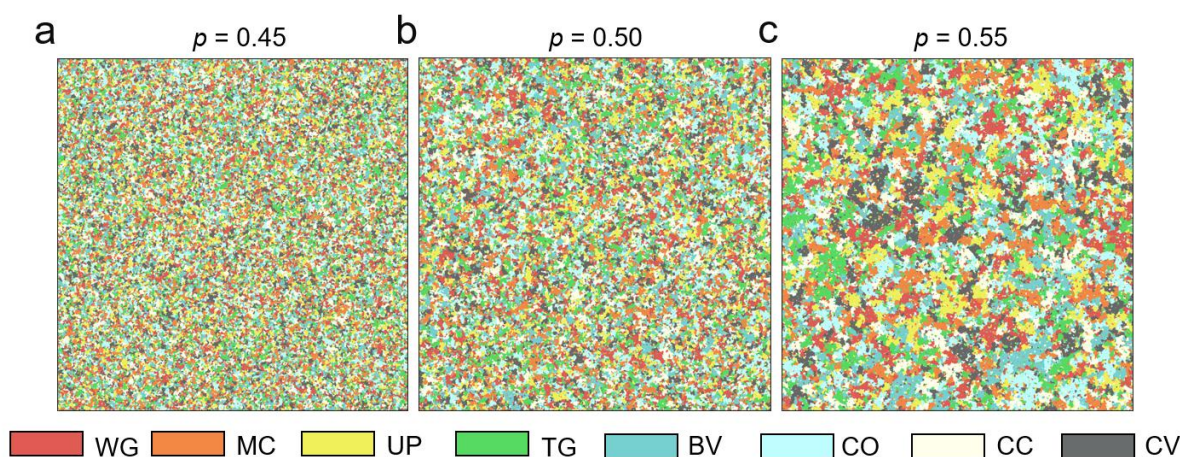

Figure 4. The simulation images from SIMMAP software with different degrees of landscape fragmentation represented by *p* values of 0.45, 0.50, and 0.55.
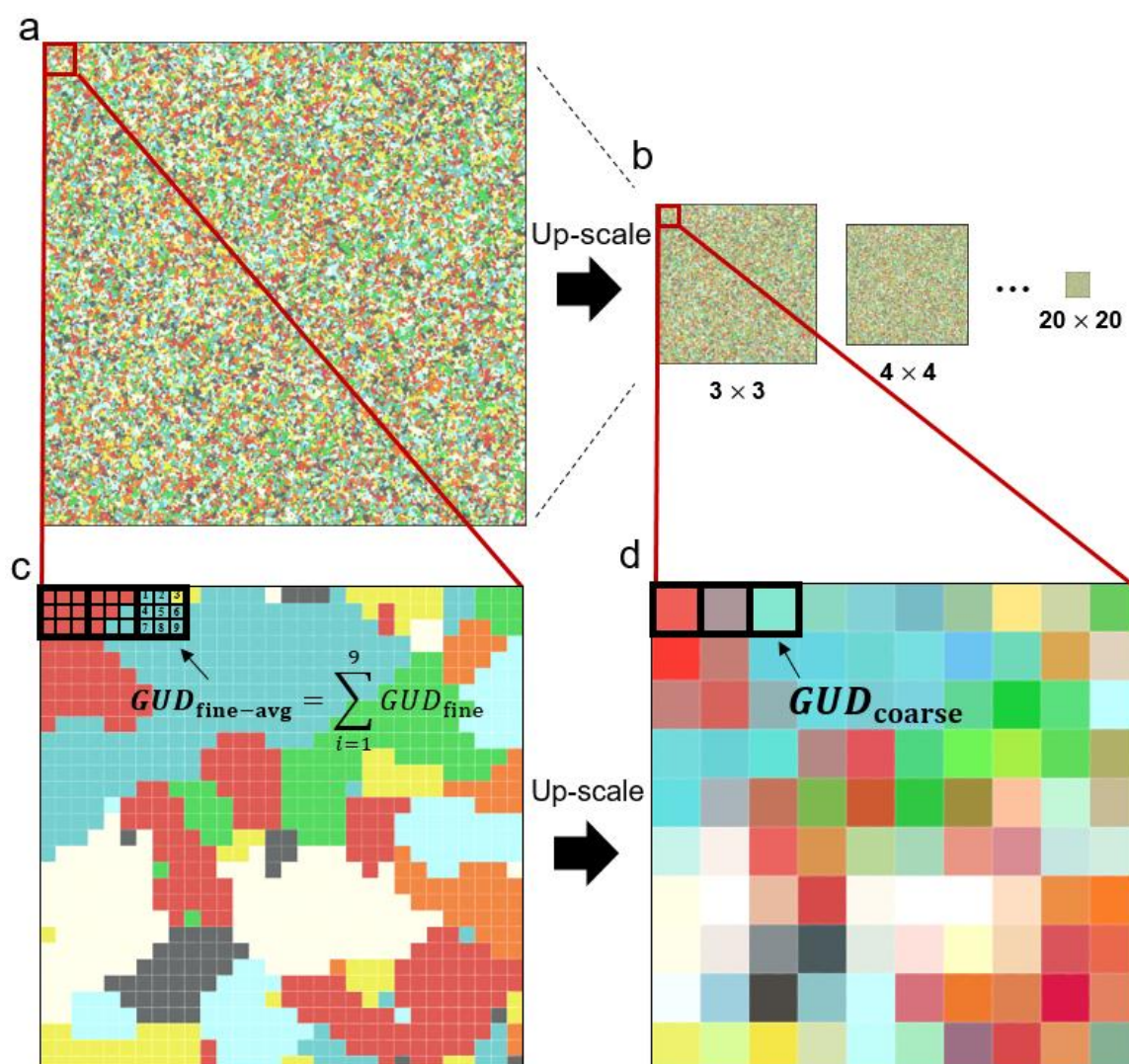
Figure 5. Up-scaling from the fine resolution images to coarser images: (**a**) fine resolution image, (**b**) up-scaled coarser images at different scales. (**c**,**d**) The example of up-scaling of 3 × 3 pixels and the corresponding calculation of $GUD_{fine-ave}$ and GUD_{coarse}.

3.2. Testing the Multi-Endmember Model Based on Landsat-MODIS Fused EVI2 Data

We further employed the same satellite data used by Zhang et al. [5] to test the multi-endmember model. The GUD_{fine} image (Figure 6) was estimated form Landsat-MODIS fused EVI2 (a two-band EVI [24]) in 2014 with a spatial resolution of 30 m and a frequency of 3 days. The study area was in central Iowa, USA, and mainly includes nine land-cover types: corn, soybean, hay, other crops, grass, forests, shrubs, non-vegetated areas, and open water/wetlands. More detailed information regarding the data was reported by Zhang et al. [5].
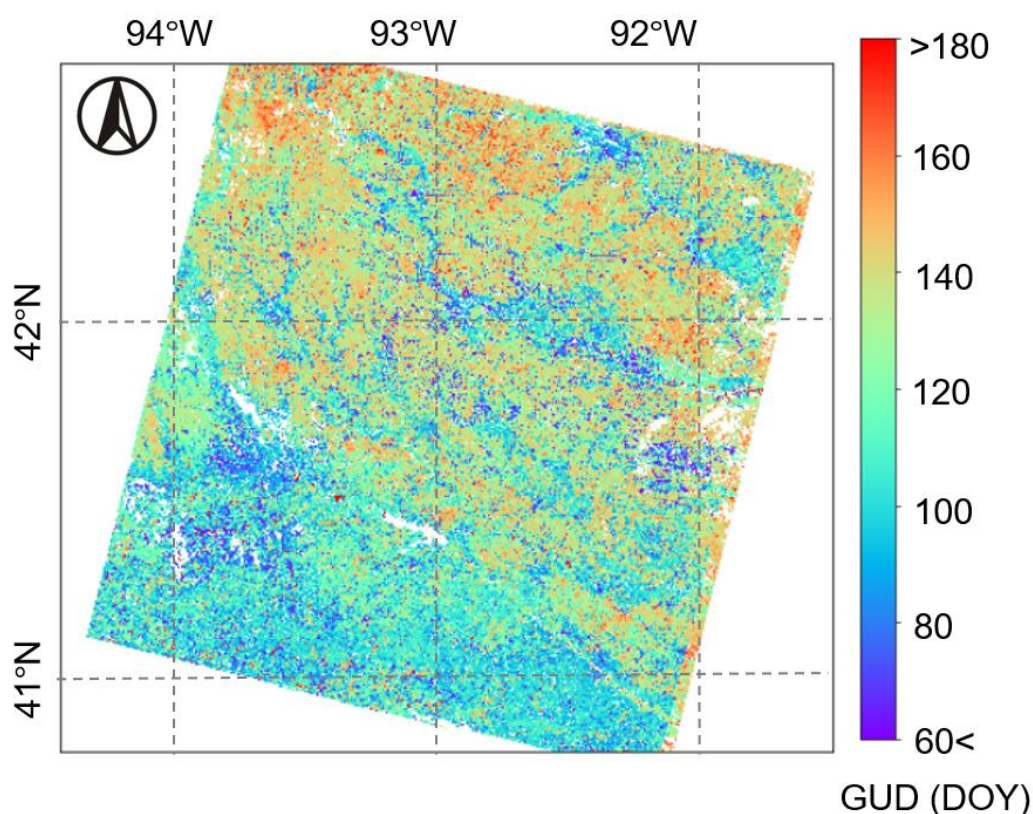
Figure 6. The *GUD* detected from fine resolution MODIS-Landsat fused EVI2 images.

Likewise, we simulated coarser satellite images by up-scaling the EVI2 data from 30 m to 150, 210, 270, 330, 390, and 450 m, which corresponds to aggregation rates of 5 × 5, 7 × 7, 9 × 9, 11 × 11, 13 × 13, and 15 × 15, respectively. During this process, we excluded some pixels with missing observations or inaccurate phenology estimations, as suggested by Zhang et al. [5]. Up-scaling operations can avoid the errors caused by geometric registration, atmospheric effect, and sensor differences, which allowed us to focus on the scale effect rather than other factors. We again randomly selected two-thirds of the pixels as training data and the remaining pixels were used for validation.

4. Results

4.1. Performance of the Two-Endmember Model

Performance of the two-endmember scale-effect model on 28 mixed *GCC* curves is shown in Figure 7. It can be seen that the two-endmember model achieved good performance (R^2_{adj} = 0.826, RMSE = 5.53 days), suggesting its ability to account for the scale effect (Figure 7a). Linear models with only one factor performed poorly, with R^2_{adj} < 0.2 and RMSE > 12 days (Figure 7b–d). These investigations emphasized that integrating the three influential factors with a proper function form is very important for explaining the scale effect.
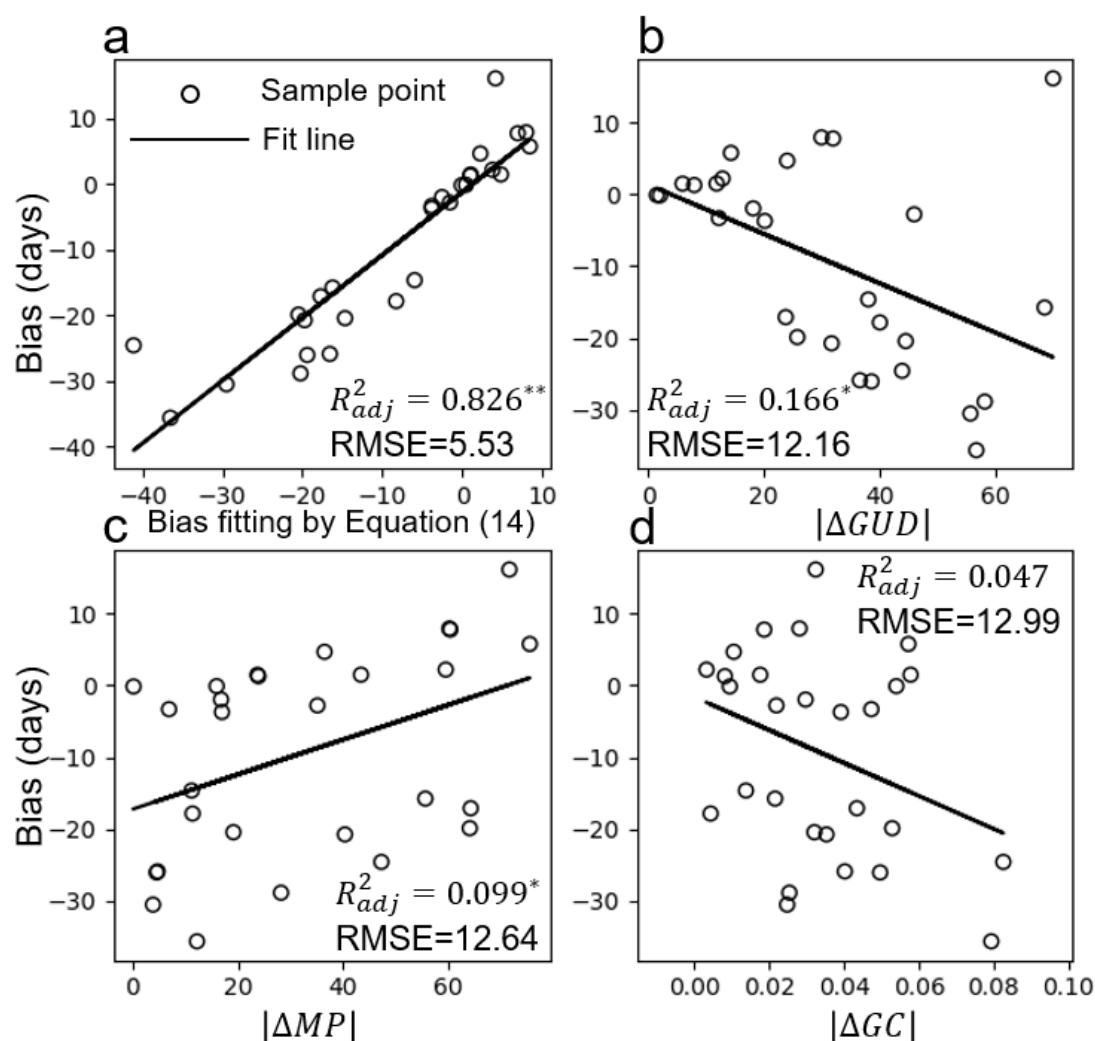
Figure 7. (**a**) Model fitting using the two-endmember model (Equation (14)) and (**b**–**d**) linearly fitting using only one of the three influential factors. Note that the bias is unrelated to the sign of the factor in three linear factor models, so we used the absolute values of the factors in (**b**–**d**) to not account for their signs. ** $p < 0.01$, * $p < 0.05$.

4.2. Performance of Multi-Endmember Model Based on SIMMAP Simulated Data

We showed the changing patterns of the average of bias ($\overline{\text{bias}}$) values at different scales for the training and validation datasets, respectively (Figure 8a,d). The average of bias (negative values) decreases as scale becoming coarser under all conditions of landscape fragmentation (p = 0.45, 0.50, and 0.55), suggesting a greater scale effect for larger differences of spatial resolution between images. Moreover, we found larger absolute values of $\overline{\text{bias}}$ in the image with higher landscape fragmentation (i.e., lower p values), which suggests that the scale effect is more obvious in heterogeneous areas. We used the proposed multi-endmember model to fit the bias values and achieved $R^2 > 0.6$ for all landscapes, both for training and validation data (Figure 8).
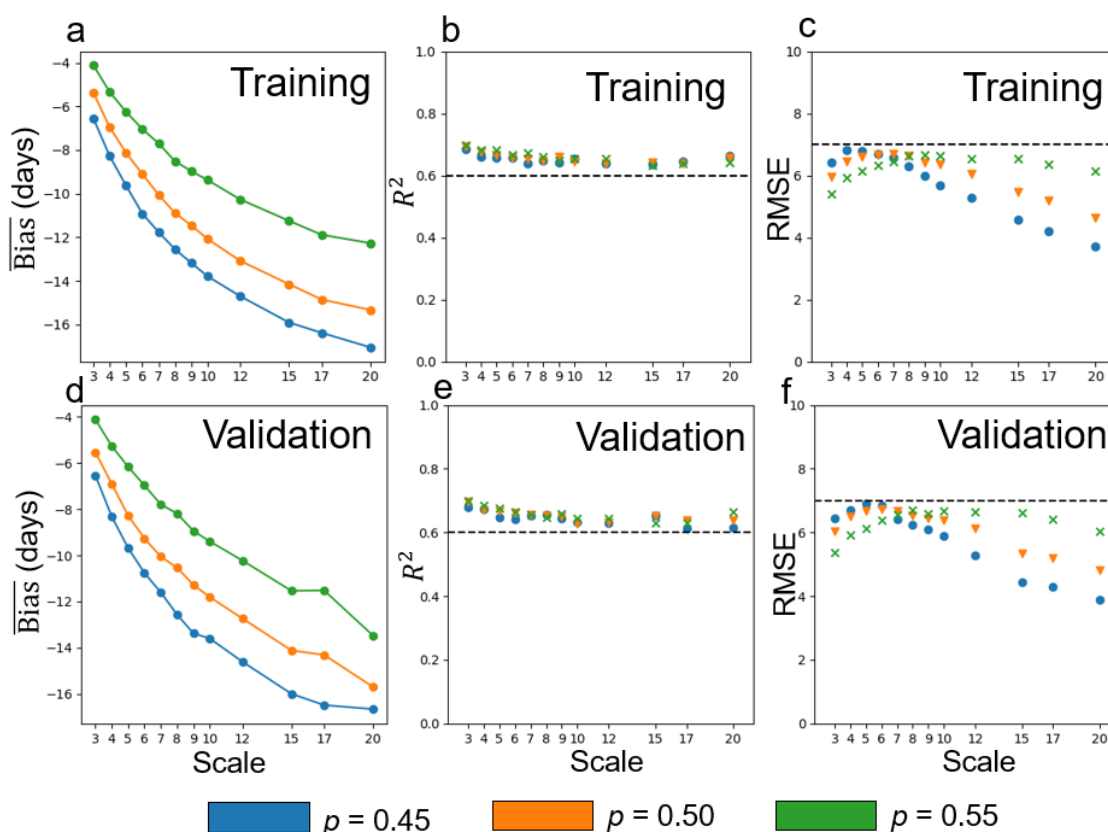
Figure 8. (**a**,**d**) The average of bias values change as the training and validation dataset scale (size of the aggregated window) changes; (**b**–**f**) Performance of the multi-endmember model at different scales for training and validation datasets in terms of the R^2 and root-mean-square error (RMSE, days) values.

4.3. Performance of Multi-Endmember Model Based on MODIS-Landsat Fused EVI2 Data

We presented the average of bias values at various scales of Landsat-MODIS fused EVI2 images in Figure 9a,d. We found a similar decreasing pattern at the larger scale, as that in Figure 8, which confirms a more considerable scale effect when the spatial resolution became coarser. We fitted these bias values by using our multi-endmember model and achieved the performance with $R^2 > 0.56$ and RMSE < 2.3 days. Taking 450-m resolution as an example, we showed the scatter plot (1:1 line) of bias and predicted bias in Figure 10. An $R^2 > 0.70$ in the validation dataset was achieved by the proposed model. Furthermore, in addition to the negative bias values, the model can also account for the positive bias values (Figure 10), suggesting that the new model can explain the delayed GUD_{coarse}, which was not well understood in previous studies [6].
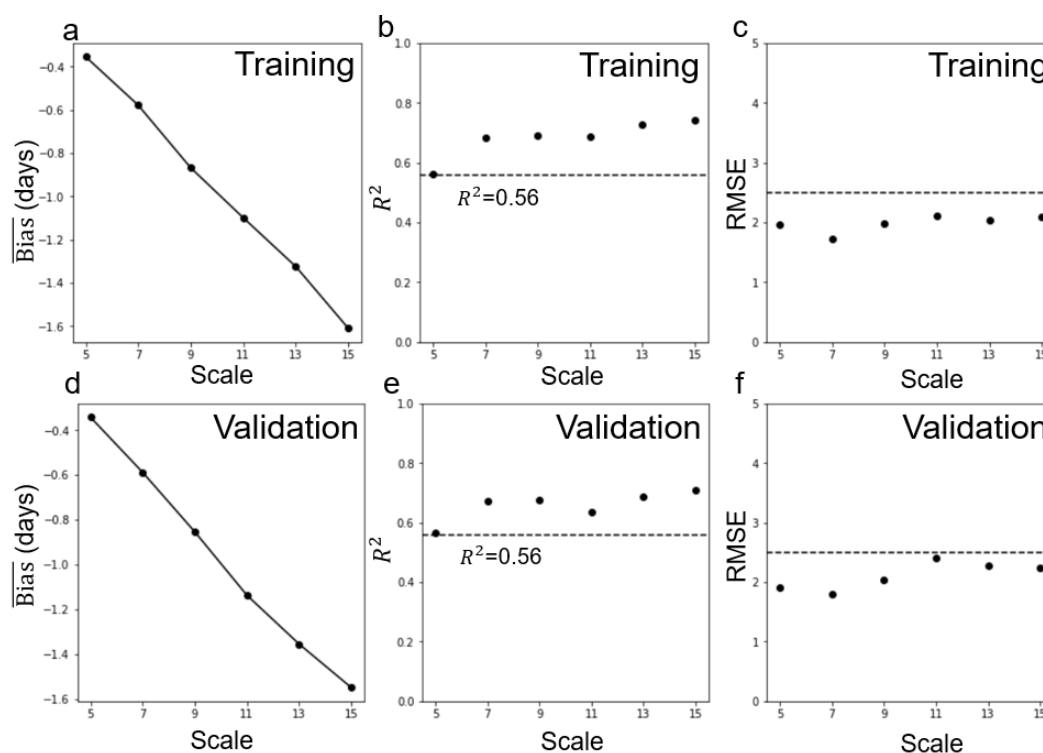
Figure 9. The same as Figure 8, but for the Landsat-MODIS fused EVI2 data. Scale refers to the size of the aggregated window.
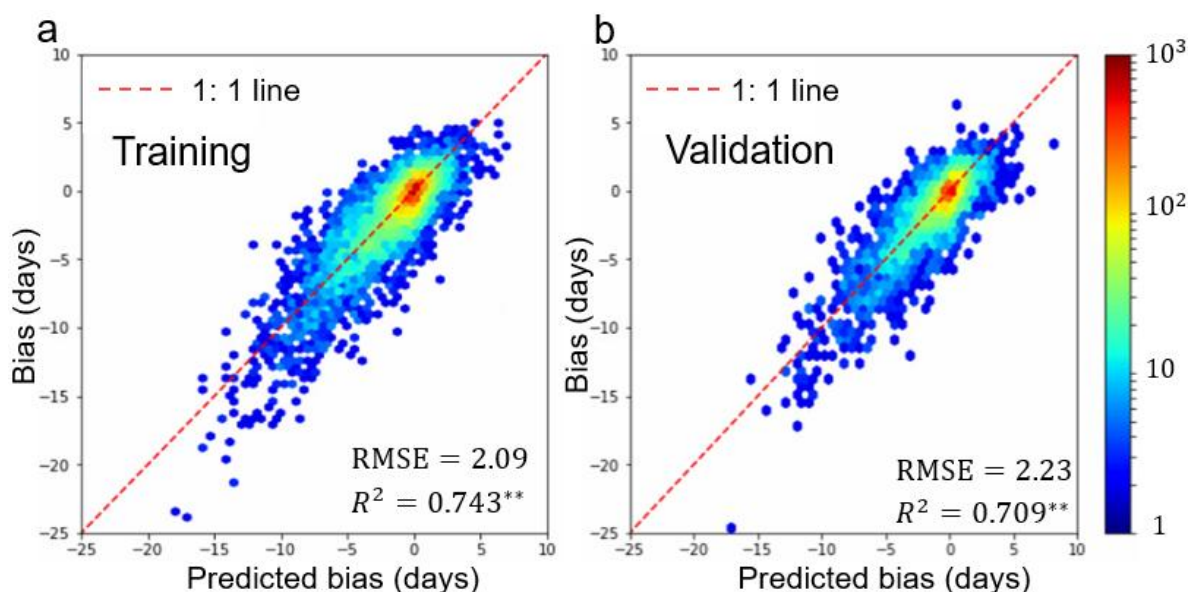

Figure 10. Performance of the multi-endmember model at the scale of 450-m resolution for the (**a**) training dataset (**b**) and validation dataset. ** $p < 0.01$.

5. Discussion

5.1. Conceptual Explanations of the Scale Effect

Previous studies attributed the scale effect of detected *GUD* to the heterogeneity of land cover or *GUD* [5,6]. However, in this study, we found that the scale effect is explained by the heterogeneities both of *GUD* and vegetation growth speed during spring. We further incorporated these factors into the scale-effect model (Equation (15)) that we developed. The good performance of the model in a series of experiments provided the rationale for clarifying these influential factors. Here, we further demonstrated in detail why the scale effect is influenced by these three factors and

how they can be used to explain some phenomena of caused by scale effect (i.e., the scale effect increases with up-scaling and GUD_{coarse} maybe later than $GUD_{\text{fine−ave}}$ in some areas).

First, we graphically explain why the detected *GUD* at a coarse pixel is earlier than the average of *GUD*s of all fine pixels within it, a phenomenon reported recently [5], and further why this tendency is stronger with greater heterogeneity of *GUD*. We simulated two coarse pixels (pixels A and B in Figure 11a,b) by the linear spectral mixture model, in which the average *GUD*s of fine pixels are identical and all the *VI* curves of corresponding fine pixels have exactly the same shape (no difference in *GC* and *MP*) but have differences in *GUD* and their proportions. The heterogeneity of *GUD* for pixel B is larger than that for pixel A (bottom-right insets of Figure 11a,b). It can be observed that the *VI* curve for pixel B with greater *GUD* heterogeneity obviously increases earlier in spring than pixel A, and thus, pixel B has an earlier *GUD* (Figure 11c). Such an advance (negative bias) is mainly because the larger number of fine pixels with earlier *GUD* in pixel B makes a greater contribution to *VI* values of the mixed coarse pixel in spring, by the linear spectral mixture model. This simulation experiment highlights that the spectral mixture process in *VI* can linearly propagate the heterogeneity of *GUD* from the fine scale to the coarse scale, leading to a significant scale effect.
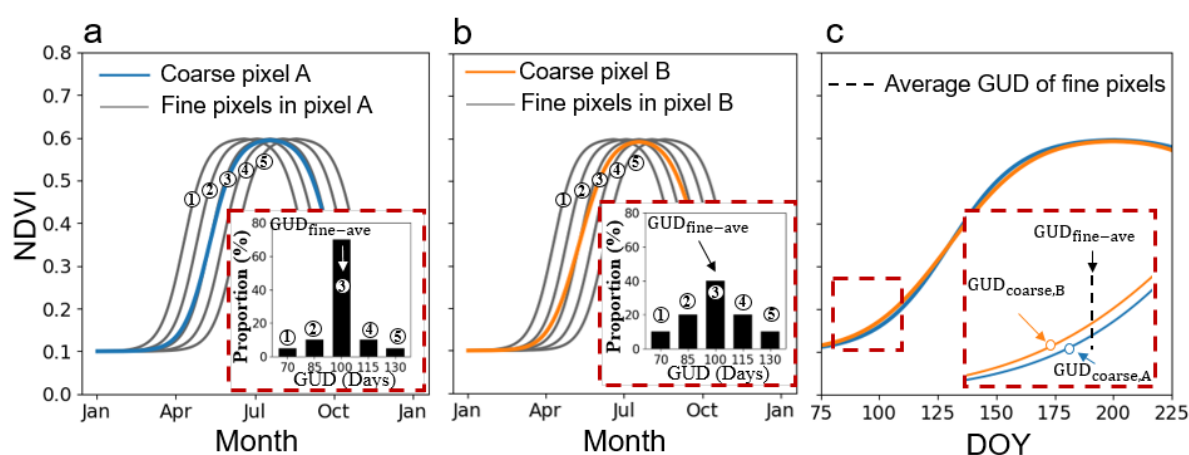

Figure 11. A simulation experiment is designed to help understand the influence of heterogeneity of *GUD* on scale effect. (**a**,**b**) Coarse pixels A and B consist of five fine *VI* curves with five different *GUD* values but the same *VI* curve shape. However, the shape of the coarse *VI* curves is different from the shape of fine *VI* curves. The heterogeneity of *GUD* is larger in pixel B than that in pixel A, as shown by the histograms of fine pixel *GUD* in the bottom-right; (**c**) The *VI* curves for coarse pixels A and B derived from the linear spectral mixture model, respectively. $GUD_{\text{coarse,B}}$ is earlier than $GUD_{\text{coarse,A}}$ and they are both earlier than $GUD_{\text{fine−ave}}$ (the vertical dashed line in the right of $GUD_{\text{coarse,A}}$).

Next, we demonstrated why heterogeneity of *MP* and *GC* under the condition of *GUD* heterogeneity can also influence the scale effect. We simulated three coarse pixels (pixels A, B, and C; black lines in Figure 12a, 12b and 12c, respectively) consisting of two fine pixels with different *GUD*s (blue and orange curves). The three coarse pixels have identical *GUD*s of corresponding fine pixels, but the later green-up fine pixel (orange line) in pixels B and C has smaller *MP* or greater *GC*. It is clear that the fine pixels with smaller *MP* or greater *GC* have greater amplitude of K' (orange lines in Figure 12e,f). Consequently, the fine pixel with greater K' values caused by greater growth speed (smaller *MP* or greater *GC*) contributes more in the K' mixing process, making the *GUD* of pixel B or C later than that of pixel A and closer to that of the later fine pixel with faster growth speed and greater K' value (Figure 12b,d). Combining Figures 11 and 12, it is clear that the heterogeneity of *GUD*, *MP*, and *GC* leads to scale effect from the fine to coarse scales through the linear mixture process both in *VI* and K', meaning that the larger the heterogeneity of the three factors, the more significant the scale effect.
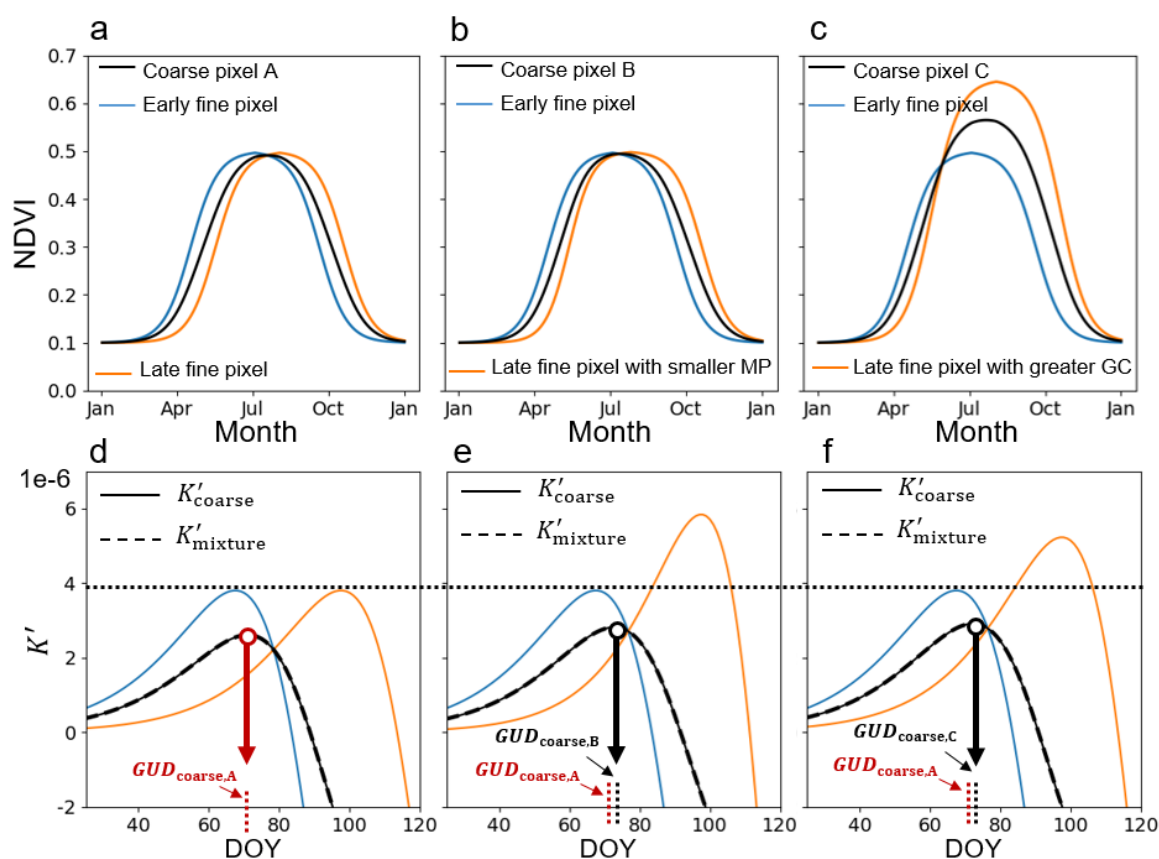
Figure 12. A simulation experiment is designed to help understand the influence of heterogeneity of growth speed on scale effect. (**a–c**) The coarse *VI* curves (black curves) mixed by two fine *VI* curves (blue and yellow curves) with the same ΔGUD_{fine} but different ΔMP_{fine} or ΔGC_{fine} (to represent different growth speeds); (**b–d**) The corresponding change rate of curvature (K') of these *VI* curves. The K' of coarse curves (black solid lines) is approximated by linear mixing of two K' values of fine curves (black dashed lines).

Our findings are based on the *GUD* detected by the curvature method. Here, we further used the widely-used relative threshold method (10% and 20% relative threshold) to estimate *GUD* and investigated whether the scale effect can still be accounted for by the three proposed factors (i.e., ΔGUD, ΔMP, and ΔGC). We performed the same experiments as those in Figure 2, and found that the relationship between the *GUD* bias and the three factors (Figures 13) was similar to those based on the curvature method (Figure 2d–f). Nevertheless, we observed that the range of the change in the bias with respect to those three factors based on the relative threshold method seems to be slightly smaller than that based on the curvature method. For example, when ΔGUD varies between −20 and 20 days, the change of the bias values caused by ΔGUD are 3 and 2.5 days for the curvature method and the relative threshold method, respectively (comparing Figure 2d–f with Figure 13). These small differences are probably because the relative threshold method is slightly less sensitive to scale effects, compared with the curvature method [11]. The scale effects on *GUD* estimated using the relative threshold method can also be explained by the three factors proposed in this study.
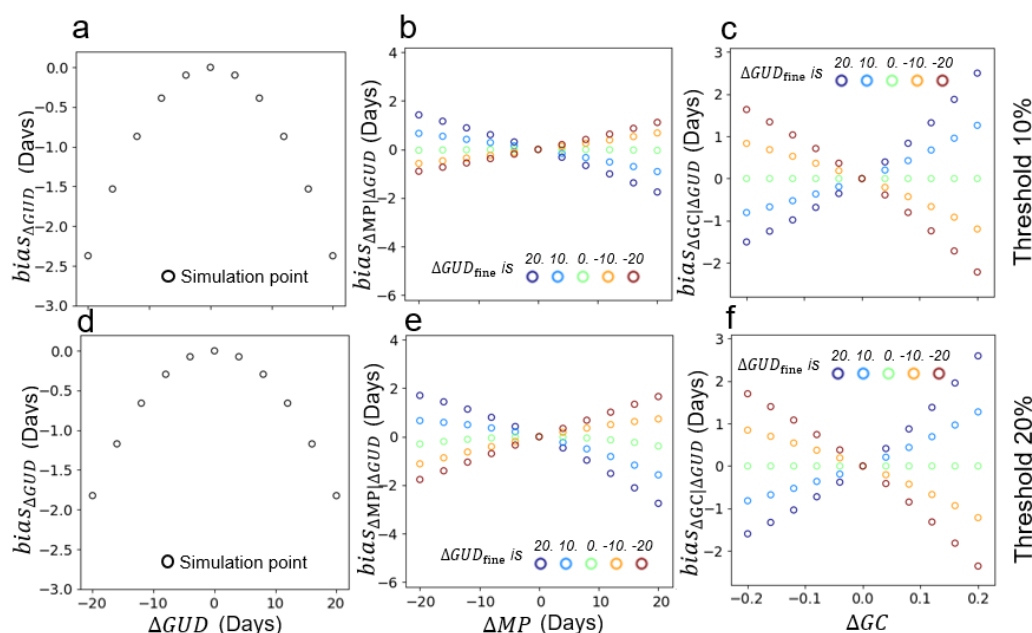
Figure 13. The same as Figure 2d–f, but using the relative threshold method. (**a–c**) $bias_{\Delta GUD_{fine}}$, $bias_{\Delta MP_{fine}|\Delta GUD_{fine}}$, and $bias_{\Delta GC_{fine}|\Delta GUD_{fine}}$ change with the corresponding factors with 10% relative threshold. (**d–f**) The same as Figure 13a–c, but using different relative threshold (20%). For comparison, the range of *Y*-axis is consistent with that in Figure 2d–f.

We conducted an up-scaling experiment over the contiguous United States. Our results confirmed the findings in Peng et al. [6] and also found that GUD_{coarse} occurred later in the processing of up-scaling in some area, which indicates a positive bias (later green-up for coarse pixel; Figures 7 and 10). The influence of growth speed of the fine-pixel *VI* curve may explain these observations. As we discussed earlier, the scale effect is caused by two kinds of biases (Equation (10)), which are accounted for by the heterogeneity of *GUD* and that of growth speed, respectively. The bias due to *GUD* heterogeneity is systematically negative (earlier green-up for coarse pixel), but the sign of the second bias depends on whether the change of *GUD* and growth speed is synchronous. In other words, when the growth speed of vegetation with later *GUD* is significantly greater than that with early *GUD*, the heterogeneity of growth speed will lead to a positive bias and even exceed the advanced effect caused by the negative former bias, eventually resulting in a positive bias. Therefore, our study highlights the importance to consider the heterogeneity of the growth speed of vegetation in the *GUD* up-scaling method, rather than to only consider the heterogeneity of *GUD*. For example, the spatial variability in the threshold of percentile method [5], observed by Peng et al. [7], may be caused by ignoring the heterogeneity of growth speed.

5.2. Implications and Limitations

Understanding the scale effect of the *VI* on *GUD* detection is useful for cross-scale comparisons and validation of satellite *VI*-derived phenology. Considering the coarse spatial resolution of commonly used *VI* products, which ranges from 250 m to 8 km, heterogeneity inevitably exists for most of the Earth's land surface and consequently leads to significant discrepancy among cross-scale comparisons and validations [5,25].

Our analyses suggest that it is helpful to reduce uncertainty to perform cross-scale phenology validation or evaluation of remote-sensing retrieval of phenology based on observations of a homogenous land surface in terms of the influential factors (i.e., the heterogeneity of *GUD*, *MP*, *GC*). For a heterogeneous surface, a practical solution is to include the scale effect in the process of comparison or validation. Table 2 lists a set of coefficients of the proposed scale-effect model for both simulation data (taking *p* = 0.5 as an example) and Landsat-MODIS fused EVI2 data. The standardized coefficients indicate the different importance of each item, and the unstandardized coefficients values are relatively stable across scales for different surfaces, suggesting the possibility

of estimating scale-derived bias, once we have developed the model for different surfaces. Accordingly, the scale-derived bias estimation will provide a reference that excludes the scale effect or will help estimate uncertainty.

Table 2. The model coefficients (c_1, c_2, c_3) in simulation data (taking p = 0.5 as an example) and Landsat-MODIS fused EVI2 data. Scale refers to the size of the aggregated window.

Type	Scale	c_1		c_2		c_3	
		Standardized	Unstandardized	Standardized	Unstandardized	Standardized	Unstandardized
Simulation data (p = 0.5)	3	−0.76	−0.035	−0.61	−0.031	0.29	14.5
	4	−0.73	−0.035	−0.60	−0.030	0.30	14.6
	5	−0.72	−0.035	−0.60	−0.030	0.31	14.7
	6	−0.72	−0.035	−0.62	−0.029	0.30	15.0
	7	−0.72	−0.036	−0.61	−0.030	0.30	14.8
	8	−0.71	−0.037	−0.60	−0.032	0.32	13.6
	9	−0.73	−0.036	−0.63	−0.030	0.33	14.7
	10	−0.72	−0.035	−0.62	−0.029	0.33	14.9
	12	−0.75	−0.036	−0.65	−0.029	0.31	15.0
	15	−0.75	−0.036	−0.64	−0.029	0.34	15.2
	17	−0.78	−0.037	−0.64	−0.029	0.33	14.4
	20	−0.90	−0.036	−0.78	−0.029	0.28	14.8
Landsat-MODIS fused data	5	−1.68	−0.037	−1.36	−0.032	0.23	1.61
	7	−1.84	−0.039	−1.45	−0.033	0.27	1.69
	9	−1.72	−0.039	−1.29	−0.033	0.25	1.71
	11	−1.67	−0.038	−1.24	−0.032	0.24	1.58
	13	−1.71	−0.039	−1.25	−0.033	0.25	1.69
	15	−1.70	−0.040	−1.23	−0.034	0.26	1.78

In the temperature-limited biomes (e.g., temperate forests), green-up of a plant species mainly depends on whether the accumulated spring temperature required for green-up is satisfied or not [26,27]. For a heterogeneous surface, the accumulated temperatures required by various species can be quite different [28,29], which may lead to substantial *GUD* heterogeneity. However, such *GUD* heterogeneity can vary among years due to temperature fluctuation, even if the vegetation community composition remains unchanged. In years with a warmer spring, the more favorable temperature conditions and faster temperature increase can make it easier to satisfy the requirements of accumulated temperature for different species. Thus, *GUD* heterogeneity among species may be reduced in these years [30]. Accordingly, it is reasonable to speculate that the heterogeneity of *GUD* within a coarse pixel could be smaller in years with a warmer spring than in those with a colder spring. Consequently, validation performed in warmer spring years may be less affected by the scale effect. Therefore, we recommend using data in warmer spring years to conduct validation. Moreover, such interannual variations of scale effect caused by different *GUD* heterogeneity could further contribute to the phenological temporal changes in heterogeneous areas. In particular, the advance of remotely sensed *GUD* under climatic warming in recent decades [31] could have been partly underestimated, because the negative bias of *GUD* caused by its heterogeneity in warmer years is smaller than the colder years. This point should be addressed when analyzing the response of phenology metrics to climate change for ecosystems detected by coarse *VI* products.

We recognize that our current scale-effect analyses still have some limitations. First, our analyses used the logistic function to describe vegetation growth. However, *VI* time-series data may deviate much from curve of logistic function in some cases (e.g., Figure 3) due to the constraints of various environmental conditions on vegetation growth [32]. Fortunately, the performance of our model in these cases seems to be acceptable (Figures 7 and 8). Further evaluations for scale effect in the case with non-logistic *VI* curve are necessary in future studies. Second, our investigations were based on up-scaled data rather than on coarse and fine data from different sensors. We did this because various errors from different sensors could not be excluded in the scale-effect analyses, such as differences in imaging conditions, band design and spectral response functions of sensors, and geometric registration, among others. Third, satellite-derived phenology metrics were detected from

VI time-series data. Some *Vi*s, such as NDVI, have several known flaws, especially with sensitivity to soil background and spring snowmelt, saturation at moderate to high greenness, and nonlinear scaling [33–35]. Clarifying the effects of these complex confounding factors may be needed in future studies to further improve our understanding of the scale effect of land-surface phenology.

6. Conclusions

Our analyses revealed that the scale effect of *GUD* was controlled by the heterogeneities of both GUD_{fine} and the vegetation growth speed (MP_{fine} and GC_{fine}) rather than land-cover or vegetation types. We developed a multivariate scale-effect model (Equation (15)) to account for the *GUD* bias across different scales. Using both simulated data and MODIS-Landsat fused EVI2 data, we confirmed that the heterogeneity of GUD_{fine} is the most important factor driving the scale effect and this factor directly causes systematically negative bias (i.e., GUD_{coarse} is smaller than $GUD_{fine-ave}$). The heterogeneity of vegetation growth speed makes the GUD_{coarse} closer to the *GUD* of vegetation with faster growth, and the direction of the effect (positive or negative bias) depends on whether there is synchronous change in the *GUD* and growth speed. Our findings provide a mechanistic explanation of the correlation between the scale effect and land-surface heterogeneity, as well as a reference to understand or further convert *GUD* acquired at different spatial resolutions.

Conflicts of Interest: The authors declare no conflict of interest.

Appendix A

For a logistic curve (Equation (A1)), based on the study of Shang et al. [17], the *GUD* derived from the curvature method can be approximately represented as:

$$GUD = \frac{\log_e(5+2\sqrt{6})-a}{b}, \tag{A1}$$

Moreover, Equation (A1) can be converted to the following form:

$$VI(t) = \frac{c}{1+e^{b(t+\frac{a}{b})}} + d, \tag{A2}$$

where $t = -\frac{a}{b}$ can represent the median point of the logistic curve, because of the symmetry of *GUD* and maturity date (*MD*) at the median point. We can obtain *MP* (*MD* − *GUD*) as:

$$MP = \left(-\frac{a}{b} - \frac{\log_e(5+2\sqrt{6})-a}{b}\right) \times 2 = \frac{-2\log_e(5+2\sqrt{6})}{b}. \tag{A3}$$

By combining Equations (A1) and (A3), a and b can be easily solved as follows:

$$b = \frac{-2\log_e(5+2\sqrt{6})}{MP}.$$

$$a = \log_e(5+2\sqrt{6}) - GUD \times b = \log_e(5+2\sqrt{6}) \times \left(1 + \frac{2GUD}{MP}\right). \tag{A4}$$

Parameter c represents the range from the maximum *VI* to the minimum *VI*. Thus, it can be directly replaced by *GC* as follows:

$$c = GC. \tag{A5}$$

References

1. Badeck, F.W.; Bondeau, A.; Bottcher, K.; Doktor, D.; Lucht, W.; Schaber, J.; Sitch, S. Responses of spring phenology to climate change. *New Phytol.* **2004**, *162*, 295–309.

2. Ganguly, S.; Friedl, M.A.; Tan, B.; Zhang, X.; Verma, M. Land surface phenology from MODIS: Characterization of the Collection 5 global land cover dynamics product. *Remote Sens. Environ.* **2010**, *114*, 1805–1816.

3. Zhang, X.; Liu, L.; Dong, Y. Comparisons of Global Land Surface Seasonality and Phenology Derived from AVHRR, MODIS and *VI*IRS Data: Phenology from AVHRR, MODIS and *VI*IRS. *J. Geophys. Res. Biogeosci.* **2017**, *122*, 1506–1525.

4. Shen, M.; Zhang, G.; Nan, C.; Wang, S.; Kong, W.; Piao, S. Increasing altitudinal gradient of spring vegetation phenology during the last decade on the Qinghai–Tibetan Plateau. *Agric. For. Meteorol.* **2014**, *189–190*, 71–80.

5. Zhang, X.; Wang, J.; Gao, F.; Liu, Y.; Schaaf, C.; Friedl, M.; Yu, Y.; Jayavelu, S.; Gray, J.; Liu, L. Exploration of scaling effects on coarse resolution land surface phenology. *Remote Sens. Environ.* **2017**, *190*, 318–330.

6. Peng, D.; Zhang, X.; Zhang, B.; Liu, L.; Liu, X.; Huete, A.R.; Huang, W.; Wang, S.; Luo, S.; Zhang, X.; et al. Scaling effects on spring phenology detections from MODIS data at multiple spatial resolutions over the contiguous United States. *ISPRS J. Photogramm. Remote Sens.* **2017**, *132*, 185–198, doi:10.1016/j.isprsjprs.2017.09.002.

7. Peng, D.; Chaoyang, W.; Xiaoyang, Z.; Yu, L.; Huete, A.R.; Wang, F.; Luo, S.; Liu, X.; Zhang, H. Scaling up spring phenology derived from remote sensing images. *Agric. For. Meteorol.* **2018**, *256–257*, 207–219.

8. Duchemin, B.T.; Goubier, J.; Courrier, G. Monitoring phenological key stages and cycle duration of temperate deciduous forest ecosystems with NOAA/AVHRR data. *Remote Sens. Environ.* **1999**, *67*, 68–82.

9. Schwartz, M.; Reed, B. Surface phenology and satellite sensor-derived onset of greenness: An initial comparison. *Int. J. Remote Sens.* **1999**, *20*, 3451–3457.

10. Wang, H.; Liu, D.; Lin, H.; Montenegro, A.; Zhu, X. ND*VI* and vegetation phenology dynamics under the influence of sunshine duration on the Tibetan plateau. *Int. J. Climatol.* **2015**, *35*, 687–698.

11. Chen, X.; Wang, D.; Chen, J.; Wang, C.; Shen, M. The mixed pixel effect in land surface phenology: A simulation study. *Remote Sens. Environ.* **2018**, *211*, 338–344, doi:10.1016/j.rse.2018.04.030.

12. Fisher, J.I.; Mustard, J.F. Cross-scalar satellite phenology from ground, Landsat, and MODIS data. *Remote Sens. Environ.* **2007**, *109*, 261–273, doi:10.1016/j.rse.2007.01.004.

13. Zhang, X.; Friedl, M.A.; Schaaf, C.B.; Strahler, A.H.; Hodges, J.C.F.; Gao, F.; Reed, B.C.; Huete, A. Monitoring vegetation phenology using MODIS. *Remote Sens. Environ.* **2003**, *84*, 471–475.

14. Friedl, M.A.; Davis, F.W.; Michaelsen, J.; Moritz, M.A. Scaling and uncertainty in the relationship between the ND*VI* and land surface biophysical variables: An analysis using a scene simulation model and data from FIFE ☆. *Remote Sens. Environ.* **1995**, *54*, 233–246.

15. Aman, A.; Randriamanantena, H.P.; Podaire, A.; Frouin, R. Upscale integration of normalized difference vegetation index: The problem of spatial heterogeneity. *IEEE Trans. Geosci. Remote Sens.* **1992**, *30*, 326–338.

16. Kerdiles, H.; Grondona, M.O. NOAA-AVHRR ND*VI* decomposition and subpixel classification using linear mixing in the Argentinean Pampa. *Int. J. Remote Sens.* **1995**, *16*, 1303–1325.

17. Shang, R.; Liu, R.; Xu, M.; Liu, Y.; Zuo, L.; Ge, Q. xThe relationship between threshold-based and inflexion-based approaches for extraction of land surface phenology. *Remote Sens. Environ.* **2017**, *199*, 167–170.

18. Doktor, D.; Bondeau, A.; Koslowski, D.; Badeck, F.W. Influence of heterogeneous landscapes on computed green-up dates based on daily AVHRR ND*VI* observations. *Remote Sens. Environ.* **2009**, *113*, 2618–2632.

19. Richardson, A.D.; Hufkens, K.; Milliman, T.; Aubrecht, D.M.; Chen, M.; Gray, J.M.; Johnston, M.R.; Keenan, T.F.; Klosterman, S.T.; Kosmala, M. Tracking vegetation phenology across diverse North American biomes using PhenoCam imagery. *Sci. Data* **2018**, *5*, 180028.

20. Soudani, K.; Maire, G.L.; Dufrêne, E.; François, C.; Delpierre, N.; Ulrich, E.; Cecchini, S. Evaluation of the onset of green-up in temperate deciduous broadleaf forests derived from Moderate Resolution Imaging Spectroradiometer (MODIS) data. *Remote Sens. Environ.* **2008**, *112*, 2643–2655.

21. Keenan, T.F.; Darby, B.; Felts, E.; Sonnentag, O.; Friedl, M.A.; Hufkens, K.; O'Keef, J.; Klosterman, S.; Munger, J.W.; Toome, M.; et al. Tracking forest phenology and seasonal physiology using digital repeat photography: A critical assessment. *Ecol. Appl. A Publ. Ecol. Soc. Am.* **2016**, *24*, 1478–1489.

22. Wang, C.; Chen, J.; Wu, J.; Tang, Y.; Shi, P.; Black, T.A.; Zhu, K. A snow-free vegetation index for improved monitoring of vegetation spring green-up date in deciduous ecosystems. *Remote Sens. Environ.* **2017**, *196*, 1–12.

23. Saura, S.; Martínez-Millán, J. Landscape patterns simulation with a modified random clusters method. *Landsc. Ecol.* **2000**, *15*, 661–678, doi:10.1023/A:1008107902848.

24. Jiang, Z.; Huete, A.R.; Didan, K.; Miura, T. Development of a two-band enhanced vegetation index without a blue band. *Remote Sens. Environ.* **2008**, *112*, 3833–3845.

25. Liang, L.A.; Schwartz, M.D.; Fei, S.L. Validating satellite phenology through intensive ground observation and landscape scaling in a mixed seasonal forest. *Remote Sens. Environ.* **2011**, *115*, 143–157, doi:10.1016/j.rse.2010.08.013.

26. Chuine, I.; Morin, X.; Bugmann, H. Warming, Photoperiods, and Tree Phenology. *Science* **2010**, *329*, 277–278.

27. Cao, R.; Shen, M.; Zhou, J.; Chen, J. Modeling vegetation green-up dates across the Tibetan Plateau by including both seasonal and daily temperature and precipitation. *Agric. For. Meteorol.* **2018**, *249*, 176–186, doi:10.1016/j.agrformet.2017.11.032.

28. Cong, N.; Shen, M.; Piao, S.; Chen, X.; An, S.; Yang, W.; Fu, Y.H.; Meng, F.; Wang, T. Little change in heat requirement for vegetation green-up on the Tibetan Plateau over the warming period of 1998–2012. *Agric. For. Meteorol.* **2017**, *232*, 650–658, doi:10.1016/j.agrformet.2016.10.021.

29. Murray, M.; Cannell, M.; Smith, R. Date of budburst of 15 tree species in Britain following climatic warming. *J. Appl. Ecol.* **1989**, *26*, 693–700.

30. Wang, C.; Tang, Y.; Chen, J. Plant phenological synchrony increases under rapid within-spring warming. *Sci. Rep.* **2016**, *6*, 25460, doi:10.1038/srep25460.

31. Shen, M.; Cong, N.; Cao, R. Temperature sensitivity as an explanation of the latitudinal pattern of green-up date trend in Northern Hemisphere vegetation during 1982-2008. *Int. J. Climatol.* **2015**, *35*, 3707–3712, doi:10.1002/joc.4227.

32. Cao, R.; Chen, J.; Shen, M.; Tang, Y. An improved logistic method for detecting spring vegetation phenology in grasslands from MODIS E*VI* time-series data. *Agric. For. Meteorol.* **2015**, *200*, 9–20, doi:10.1016/j.agrformet.2014.09.009.

33. Huete, A.R.; Jackson, R.D. Soil and atmosphere influences on the spectra of partial canopies. *Remote Sens. Environ.* **1988**, *25*, 89–105.

34. Ding, Y.; Zheng, X.; Kai, Z.; Xin, X.; Liu, H. Quantifying the Impact of ND*VI*soil Determination Methods and ND*VI*soil Variability on the Estimation of Fractional Vegetation Cover in Northeast China. *Remote Sens.* **2016**, *8*, 29.

35. Cao, R.; Chen, Y.; Shen, M.; Chen, J.; Zhou, J.; Wang, C.; Yang, W. A simple method to improve the quality of ND*VI* time-series data by integrating spatiotemporal information with the Savitzky-Golay filter. *Remote Sens. Environ.* **2018**, *217*, 244–257, doi:10.1016/j.rse.2018.08.022.